Measurements of diffusion coefficient and kinetic diameter of acetone vapor via molecular tagging

Zongwei Zhang, Dominique Fratantonio, Christine Barrot Lattes, Marcos Rojas-Cardenas, Stéphane Colin

Microfluidics and Nanofluidics (2024) 28:62
https://doi.org/10.1007/s10404-024-02754-8

RESEARCH

Measurements of diffusion coefficient and kinetic diameter of acetone vapor via molecular tagging

Zongwei Zhang[1,2] · Dominique Fratantonio[1,2,3] · Christine Barrot Lattes[1,2] · Marcos Rojas-Cardenas[1,2] · Stéphane Colin[1,2]

Received: 29 January 2024 / Accepted: 23 July 2024

Abstract
The Molecular Tagging (MT) technique is a promising methodology for locally measuring velocity and temperature fields in rarefied gas flows. Recently, Molecular Tagging Velocimetry (MTV) has been successfully applied to gas flows in mini-channels in the continuum regime at high pressure and early slip-flow regime at lower pressure. As the operating pressure decreases, diffusion effects become more pronounced, and in MTV, they hinder the extraction of the correct velocity profile by simply dividing the displacement profile of the tagged molecular line by time of flight. To address this issue, a reconstruction method that considers Taylor dispersion was previously developed to extract the velocity profile, considering the diffusion effects of the tracer molecules within the carrier gas. This reconstruction method successfully extracted the correct velocity profile in the continuum flow regime. However, the method still faces challenges in the slip-flow regime. Since there is currently no consensus in the literature regarding the kinetic diameter value of acetone vapor, the diffusion coefficient estimation is uncertain especially at low pressures. This is why, in this study, we propose an original optical method to measure the diffusion coefficient of acetone vapor. This is achieved by linking the temporal evolution of the spatial photoluminescence distribution of acetone vapor to the diffusion coefficient via the Chapman-Enskog theory. Our research provides measurements of these parameters for a wide range of pressures (0.5–10 kPa) at ambient temperature.

Keywords Diffusion · Kinetic diameter · Molecular tagging · Photoluminescence · Acetone vapor · Gas flow

1 Introduction

In recent years, there has been a growing interest in gas microflows due to their wide range of appealing applications in microfluidics. These applications include micro heat exchangers (Rehman et al. 2020), Knudsen pumps (Zhao et al. 2023; López Quesada et al. 2019), artificial lungs (Potkay 2014), gas detectors (Vo et al. 2019), manipulation of micro-objects (Otic and Yonemura 2022) and pressure sensors (Javed et al. 2019). They span various industrial and scientific domains, including transport, healthcare, energy, environment, and aerospace.

When the dimensions of fluidic devices are reduced, rarefaction effects become significant in gases, rendering the classical boundary conditions and the continuum medium assumption invalid (Colin 2010). A gas is considered rarefied when the mean free path λ of the molecules is comparable to or larger than the characteristic length L_c of the microdevice. Under such conditions, local thermodynamic disequilibrium near the wall results in velocity slip and

✉ Stéphane Colin
stephane.colin@insa-toulouse.fr

Zongwei Zhang
zozhang@insa-toulouse.fr

Dominique Fratantonio
dfratantonio@lanl.gov

Christine Barrot Lattes
christine.barrot@insa-toulouse.fr

Marcos Rojas-Cardenas
marcos.rojas@insa-toulouse.fr

[1] Institut Clément Ader (ICA), Université de Toulouse, CNRS, INSA, ISAE-SUPAERO, Mines-Albi, UPS, Toulouse, France

[2] Fédération de Recherche FERMAT, CNRS, Toulouse, France

[3] AOT Division, Los Alamos National Laboratory, Los Alamos, USA

Published online: 09 August 2024

temperature jump, which have a considerable impact on the macroscopic velocity and temperature distributions within the flow. This study is connected to slightly rarefied gas flow conditions within the slip-flow regime, corresponding to Knudsen numbers $Kn = \lambda / L_c$ in the range of [0.001, 0.1].

A comprehensive understanding of transport phenomena at the microscale is essential for the precise design and optimization of fluidic microsystems involving gases. To achieve this, direct and local measurements are required to characterize crucial parameters, including viscosity, diffusion, and momentum and energy accommodation coefficients. These parameters are necessary for an accurate description of flow boundary (Sharipov and Seleznev 1998; Colin 2005). However, due to the limited dimensions of the investigated domain, obtaining precise measurements of velocity and temperature distributions in gas microflows is extremely challenging, especially near the wall and within the Knudsen layer (Maali et al. 2016; Colin et al. 1819). Consequently, most of the experimental studies found in the literature primarily focus on measuring global quantities, such as the mass flow rates or pressure and temperature differences between the inlet and outlet of microchannels or fluidic microsystems (Arkilic et al. 2001; Colin et al. 2004; Pitakarnnop et al. 2010; Trott et al. 2011; Rojas-Cárdenas et al. 2015; Silva et al. 2016).

Local measurements of velocity and temperature fields in gas microflows have been achieved by our research group in the past through the development of a molecular tagging (MT) technique. This technique is optical and low-intrusive, leveraging laser-induced photoluminescence (both fluorescence and phosphorescence) from specific tracer molecules seeded into the gas flow under investigation (Samouda et al. 2015; Frezzotti et al. 2015; Si Hadj Mohand et al. 2017; Fratantonio et al. 2018, 2020). Specifically, the molecular tagging velocimetry (MTV) technique involves tracking the displacement of luminescent tracer molecules over a short time interval, typically in the micro-to-millisecond range (Koochesfahani and Nocera 2007; Hu and Koochesfahani 2006). Nevertheless, it is typically preferred to perform experiments in devices with millimetric characteristic lengths in order to obtain molecular displacement profiles with high spatial resolution. To operate in the rarefaction regime of interest at this scale, that is the slip flow regime, the gas pressure must be sufficiently low, typically in the range of 0.1–1 kPa.

The MTV technique has been successfully employed to measure velocity profiles in a rectangular mini-channel in the continuum (or hydrodynamic) regime (Samouda et al. 2015; Si Hadj Mohand et al. 2017; Fratantonio et al. 2020) and the slip-flow regime (Fratantonio et al. 2020). The observed slip velocities at the wall were obtained for a helium flow seeded with acetone vapor at a pressure of approximately 1 kPa and a Knudsen number of the order of 0.01 (Fratantonio et al. 2020). However, low molecular concentrations at low pressure pose significant challenges in implementing this technique due to the weak luminescent signal and the pronounced diffusion effects.

Molecular diffusion prevents the direct extraction of the local flow velocity profile by simply dividing the molecular displacement profile by the time of flight. In the case of confined flows, this advection–diffusion effect is known as Taylor dispersion and leads to molecular displacement at the wall, even for gas flows in hydrodynamic regime, where a zero macroscopic velocity at the wall is expected. Molecules close to the wall can diffuse in regions where advection is not negligible, and after being advected along a streamline at a certain distance of the wall, they can experience diffusion in the direction of the wall, resulting finally in a displacement in the streamwise direction close to the wall. Consequently, the displacement profile in a 2-D Poiseuille flow exhibits a non-parabolic shape (Samouda et al. 2015). Therefore, a specific reconstruction algorithm (Frezzotti et al. 2015) that accounts for the combined effect of advection and diffusion is necessary to obtain an accurate extraction of the velocity profile from the measured displacement profile. This reconstruction technique has been successfully applied in the continuum regime (Si Hadj Mohand et al. 2017; Fratantonio et al. 2020), while it has not provided accurate results in slightly rarefied gas flows, specifically regarding velocity measurements at the wall (Fratantonio et al. 2020).

One possible cause can be linked to the strong sensitivity of the reconstruction algorithm to the diffusion coefficient of the molecular tracer in the background gas. The reconstruction method is based on the advection–diffusion equation, which can be written for a plane flow as:

$$\frac{\partial s_x}{\partial t} = u_x(y) + D_{2/1,2}\frac{\partial^2 s_x}{\partial y^2} \tag{1}$$

In this equation, s_x and u_x are respectively the displacement and the velocity in the direction x parallel to the wall, y is the direction perpendicular to the wall, t is time and $D_{2/1,2}$ is the diffusion coefficient of the tracer (subscript 2) in the flow mixture composed of the background gas (subscript 1) and tracer. According to Blanc's law (Blanc 1908),

$$D_{2/1,2} = \left(\frac{1-\chi_2}{D_{2/1}} + \frac{\chi_2}{D_{2/2}}\right)^{-1} \tag{2}$$

this diffusion coefficient depends on the molar fraction χ_2 of the tracer in the mixture, on the binary diffusion coefficient $D_{2/1}$ of the tracer in the pure background gas and

on the self-diffusion coefficient $D_{2/2}$ of the tracer. The self-diffusion coefficient $D_{2/2}$ and the binary diffusion coefficient $D_{2/1}$ can be approximated from the Chapman-Enskog theory as (Marrero and Mason 1972):

$$D_{2/i} = \frac{3}{8\, d_{2i}^2\, p}\sqrt{\frac{\left(k_B\, T\right)^3}{2\pi m_{2i}}} \tag{3}$$

for $i = 1$ or 2 and where k_B is the Boltzmann constant, T is the temperature, p is the pressure, $m_{2i} = \frac{m_2\, m_i}{m_2+m_i}$ is the reduced molecular mass and $d_{2i} = \frac{d_2+d_i}{2}$ is the average kinetic molecular diameter of the gas mixture, m_i and d_i being respectively the molecular mass and diameter of species i representing the background gas 1 or the molecular tracer 2.

The accurate calculation of the diffusion coefficients directly depends on the correct estimation of the kinetic diameters d_1 and d_2 of the background gas and tracer molecules. This value is generally well documented for usual background gases, such as argon or helium, that were used in previous MTV experiments. On the other hand, for acetone vapor, which is a complex molecule and one of the most widely used MT tracers, various values of d_2 can be found in the literature (Table 1). Therefore, there is still no clear consensus on the subject. This issue directly affects the estimation of the molecular diffusion coefficient $D_{2/1,2}$ estimated by Eq. 2 and necessary for implementing the reconstruction method based on Eq. 1.

For this reason, it is of crucial importance to accurately characterize the self-diffusion coefficient $D_{2/2}$ of acetone in low-pressure gas flows to improve the measurement of velocity fields through molecular tagging. The knowledge of $D_{2/2}$ will allow extracting d_2 then $D_{2/1}$ with Eq. 3 and finally $D_{2/1,2}$ with Eq. 2.

Thus, in this work, we investigate and measure the self-diffusion coefficient of acetone vapor using molecular tagging over a wide range of pressures. This paper is presented as follows: Sect. 2 provides a summary of the experimental methodology and Sect. 3 details the data post-processing method. Section 4 presents the measured results along with a discussion on the most significant intramolecular processes involved in the molecular tagging of acetone vapor. The conclusions of this work are drawn in Sect. 5.

2 Experimental setup

The primary objective of this experimental work was to visualize the self-diffusion of acetone after laser excitation inside an optically accessible chamber. Molecular tagging was used to measure the displacement of photoluminescent molecules from an initial excitation until signal extinction. Throughout one experiment, the gas was at rest with steady thermodynamic conditions. Parameters such as pressure and temperature of the tracer were carefully monitored and controlled. The schematic diagram in Fig. 1 illustrates the key components of the experimental setup: (i) gas circuit; (ii) laser beam and optics; (iii) visualization chamber; (iv) acquisition system.

Table 1 Values of kinetic diameter of gaseous acetone molecules published in the literature and corresponding self-diffusion coefficient values at $p = 1$ kPa and $T = 294$ K, computed via Eq. 3

References	d_2(pm)	$D_{2/2}$(cm^2/s)
Hu et al. (2019)	460	8.32
Frezzotti et al. (2015)	730	3.31
Nadykto and Yu (2003)	616	4.64
Bowen et al. (2004)	469	8.01
Almy and Anderson (2004)	590	5.06

The static visualization chamber was assembled using pieces in aluminum alloy, which is resistance to acetone vapor. Two coaxial accesses allowed the laser beam crossing the chamber. The optical windows were made of Suprasil®, which is a fused silica material highly transparent to UV light. This two-window design served to reduce reflections of the laser beam inside the chamber and enabled real-time control of the laser's energy using an energy detector placed at the end of the optical path. After excitation, the luminescent emitted light was collected through an optical access of Borofloat® glass located on the top side of the chamber.

The gas chamber was connected to an acetone tank at the inlet and two GEFI® rotary vacuum pumps at the outlet. To monitor the pressure inside the gas chamber, two Inficon® capacitance diaphragm sensors with different scales (P1 with a full scale of 13.3 kPa, and P2 with a full scale of 1.3 kPa) were used. Ideally, the measured pressures should remain constant. However, variations may occur due to the absorption and desorption of acetone molecules on the inner walls of the visualization chamber, as well as potential air leakages, which might slightly affect pressure stability. During one experiment, the most significant pressure variation was observed at lower pressures, with a maximum variation of $\pm 3.6\%$ relative to the nominal pressure. For pressures higher than 1.5 kPa, the variation remained consistently below $\pm 1\%$.

The visualization chamber was supplied with acetone vapor generated from a liquid acetone tank. In order to ensure acetone at the vapor state in the chamber, the static pressure was always regulated to values below the saturation vapor pressure at room temperature. The thermodynamic conditions in the inlet gas line were monitored using another capacitive diaphragm gauge, Pressure Sensor P3, with the same full scale as P1. Vacuum Pump 1 was used to evacuate gas from the visualization chamber, while Vacuum

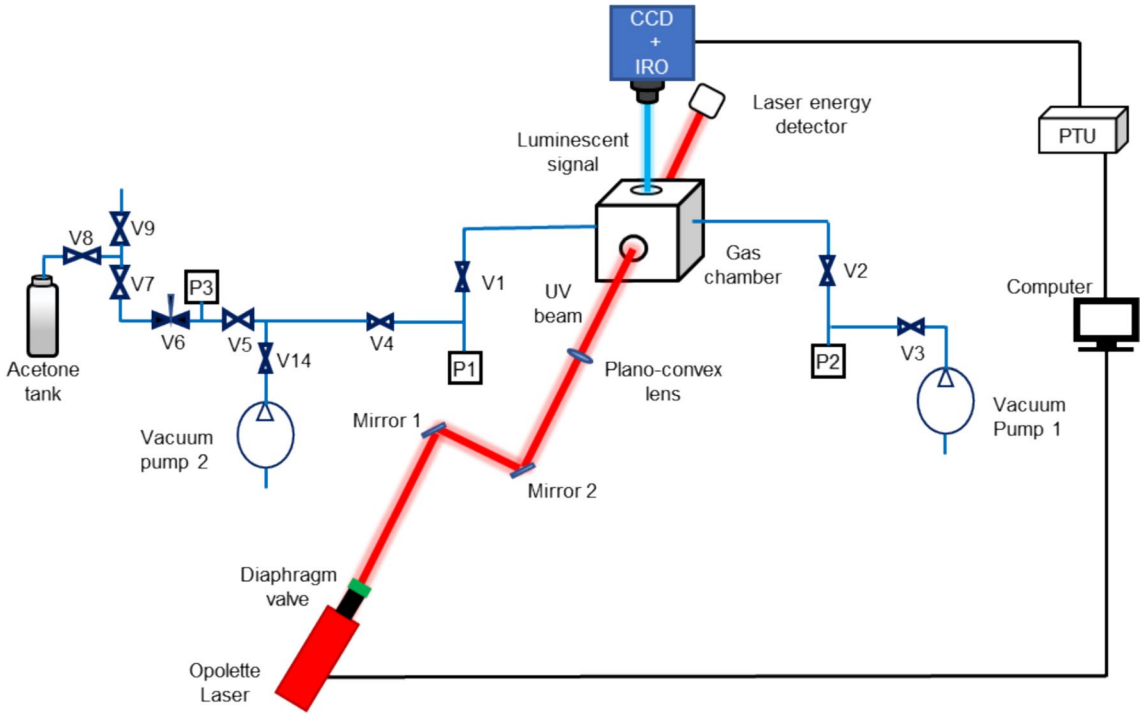

Fig. 1 Schematic of the experimental setup

Pump 2 controlled the pressure in the gas line. All the valves depicted in the illustration were Pfeiffer® globe valves, except for Valve V6, which was a HEF® dosing valve used for precisely controlling the amount of acetone vapor introduced into the gas chamber.

We utilized an OPOlette HE355LD laser operating at 310 nm to excite the molecular tracer. This tagging wavelength ensured high signal intensity and long phosphorescence lifetime (Fratantonio et al. 2018). The laser had a repetition rate of 20 Hz and emitted a laser beam collimated via a plano-convex lens to a 175 µm beam waist, calculated from the fluorescence signal distribution at the moment of laser excitation.

To align the UV beam, a pair of mirrors was positioned at 45° angle in a Z-Fold configuration. Pyroelectric laser energy detectors from Gentec-EO® were employed for real-time monitoring of the laser energy stability of the UV beam both before and after it passed through the visualization chamber. This allowed us to calculate the energy absorption attributable to the Suprasil® windows and acetone molecules. Maintaining a low laser energy was preferable to protect the integrity of the optical accesses.

The image acquisition system consisted of a photodetector equipped with a 25-mm intensified relay optics (IRO) and a 12-bit Imager Intense (LaVision®) progressive scan charge-coupled device (CCD), collectively referred to as ICCD. The ICCD comprises a series of lenses that guide light into the photodetector, including two external objectives, a 105 mm f/2.8, and an inverted 28 mm f/2.8 Micro Nikkor® lens, designed for collecting the photoluminescence emitted by the tracers within the gas chamber. The field of view (FOV) for the acquired image was 5.29 mm × 4 mm.

To increase the recorded light intensity, a 4 × 4 binning was implemented in all experiments. This resulted in a spatial resolution of 15.2 × 15.2 µm^2 per pixel. For synchronization purposes between laser shots and IRO acquisition, a programmable timing unit (PTU), with a precision of 5 ns was used. It facilitated the synchronization of the laser trigger, the camera shutter trigger, and the IRO trigger (Fratantonio et al. 2018).

3 Experimental methodology

The diffusion experiments were conducted within a static visualization chamber that was filled with acetone under stable thermodynamic conditions. The investigated pressure range spanned from 0.5 to 10 kPa, and the experiments were carried out at room temperature ($T = 294 \pm 0.5$ K). The beginning of the experiment at $t_0 = 0$ coincided with excitation of acetone molecules via the UV laser shots inside the chamber. Following excitation, the acetone tracer emits light in the visible spectrum. The luminescent signal was utilized to visualize and measure the macroscopic

displacement of the molecules. Depending on the molecular concentration, the phosphorescent emission could extend to the millisecond range, which was sufficient for measuring molecular diffusion.

After the initial tagging moment, signal acquisition occurred at delay times of 0.005 µs, 0.5 µs, 1 µs, 2.5 µs and then at 2.5 µs intervals up to 10 µs. Subsequently, measurements were taken at 10 µs intervals up to 100 µs, followed by 50 µs intervals up to 500 µs. This resulted in a total of 24 acquisitions for each experiment. It should be noted that the maximum delay times considered in these experiments were much longer than those typically used in previous MTV studies, where the maximum delay times were around 50 µs (Fratantonio et al. 2018), even for partial pressures of acetone in the gas mixture as low as 180 Pa.

The low pressures used for the experiments resulted in low concentrations of tracer molecules, leading to weak light emissions from a single laser pulse, which were insufficient for generating a significant signal (Samouda et al. 2015). To address this limitation, the on-chip integration technique was employed to accumulate emissions from multiple laser pulses within a single image, effectively extending the sensor's exposure time to light. On-chip integration, combined with the averaging of a substantial number of images, significantly increased the signal-to-noise ratio (SNR) to usable levels. In this work, each image was generated by summing the emissions from $N_l = 100$ laser shots, and each experiment involved the averaging of $N_i = 30$ such images. For each signal acquisition, the IRO amplification gain G was fixed at 100%, while the gate time, corresponding to the duration of IRO shutter opening and denoted as Δt_{gate}, was set between 0.1 and 1 µs, according to the delay time. Further details about the on-chip integration technique can be found in our previous publications (Si Hadj Mohand et al. 2017; Fratantonio et al. 2018).

As demonstrated in our previous works, the emitted signal distribution following excitation corresponds to the laser beam profile, which can be accurately described by a Gaussian distribution function. Diffusion can be linked to the luminescence distribution evolution with time of the tagged line and the Gaussian function can be written as:

$$f(x,t) = a_1(t) + \frac{a_2(t)}{\sqrt{2\,\pi\,a_3(t)}} e^{-\frac{(x-a_4)^2}{2a_3(t)}} \tag{4}$$

Here a_1, a_2, a_3, and a_4 represent the fitting parameters of the Gaussian function (Si Hadj Mohand et al. 2017), and x denotes the position along the direction perpendicular to the laser beam within the focal plane. Parameter $a_1(t)$ represents the background emission offset which is attributed to excited tracer molecules located outside the laser beam or adsorbed by the internal walls. This parameter is never zero and decreases over time. Coefficient $a_2(t)$ corresponds to the amplitude of the Gaussian signal, and its temporal evolution is closely related to the phosphorescence lifetime of the excited tracer. Additionally, the variation of this parameter over time is influenced by diffusion mechanisms. Parameter $a_3(t)$ corresponds to the variance σ_x^2 of the Gaussian function $f(x,t)$ and provides insights into the diffusion rate of the excited tracer molecules. It directly reflects how the tagged line profile broadens with time. Finally, Parameter a_4 represents the position of the Gaussian peak, which may vary slightly at each acquisition due to possible small fluctuations in the laser beam's position. These fluctuations can arise from unwanted mechanical vibrations or changes in the laser profile over time. From the Gaussian function, two parameters of interest can be defined:

i) the Gaussian peak value, which represents the highest intensity of the photoluminescence signal at each moment. It can be defined as:

$$S_{\max} = f\left(a_4, t\right) = a_1(t) + \frac{a_2(t)}{\sqrt{2\,\pi\,a_3(t)}} \tag{5}$$

and is influenced by the decay of the phosphorescence signal with time and the molecular diffusion of the excited molecules (Fratantonio et al. 2018). This peak value will serve later as a parameter to define the quality of the signal.

ii) the full width at half maximum

$$FWHM = 2\sqrt{2\ln 2}\,\sigma_x \tag{6}$$

which is directly linked to the standard deviation of the gaussian function and serves as measurement of the width of the laser beam waist at the half height in respect to the peak value.

An illustrative example of diffusion measurements at constant pressure using the molecular tagging technique at different instants is presented in Fig. 2. This optical technique enables real-time tracking of the emitted light from acetone molecules and the measurement of its evolving distribution over time due to diffusion effects. The raw acquired images are displayed in the odd-numbered rows of Fig. 2, while the post-treated Gaussian profiles are shown in the even-numbered rows. The signal was averaged along the y-direction of the laser beam for each x position. Through this method the statistical fluctuations of the light emission distribution were significantly reduced. The data in Fig. 2 was collected at a pressure of 1 kPa, under which condition the beam full width at half maximum increased from $FWHM = 175\ \mu$m at $t = 0.005\ \mu$s to $FWHM = 1376\ \mu$m at $t = 500\ \mu$s. Furthermore, the quality of the signal decreases when time increases as both phosphorescence decay and molecular diffusion reduce the light intensity. To maintain a measurable signal, the gate time Δt_{gate} was then adjusted as a function of time. It was set at 0.1 µs for times t up to 10 µs, then it was extended to 0.5 µs for times ranging from 20 to 100 µs, and further

increased to 1 µs for times exceeding 100 µs. This adjustment explains the increase in the count numbers observed between $t = 10\ \mu$s and $t = 20\ \mu$s.

The calculation of the diffusion coefficient was performed using the Einstein-Brownian motion equation, which relates the diffusion coefficient D to the time evolution of the variance of the tagged molecules' distribution:

$$\sigma_x^2(t) = 2\,D\left(t - t_0\right) + \sigma_{x,0}^2 \tag{7}$$

Here, $\sigma_x^2 = a_3(t)$ corresponds to the variance extracted experimentally from the gaussian distribution (Eq. 4) at every instant, t represents the time elapsed after the laser excitation, and $\sigma_{x,0}^2$ is the variance of the initial light distribution at $t = t_0$ (Einstein 1956). According to this equation, the

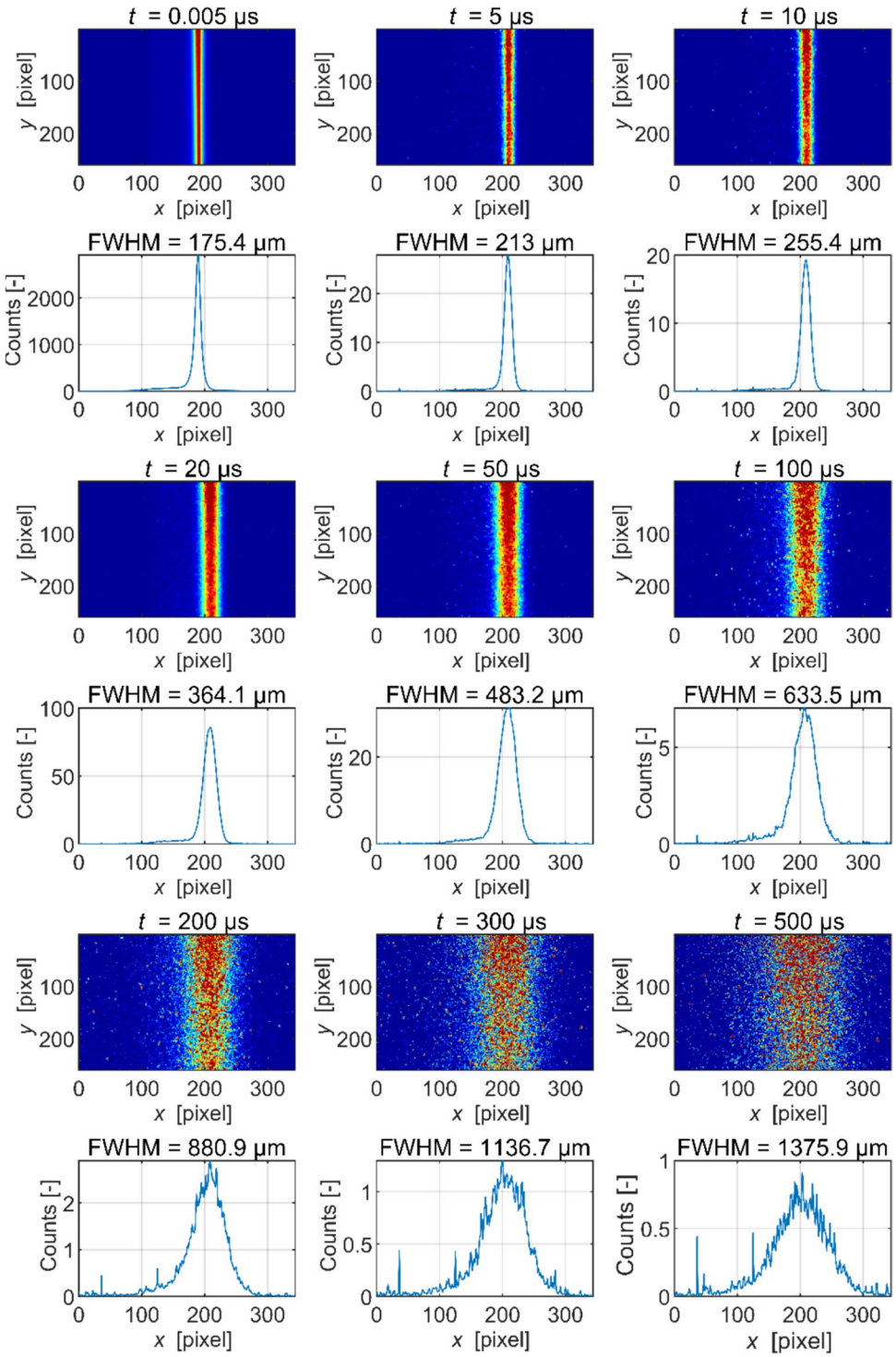

Fig. 2 Temporal evolution of photoluminescence signal images and corresponding light distribution profile (blue solid line) for $p = 1$ kPa

variance should exhibit a linear evolution over time, with a slope directly proportional to the diffusion coefficient. Consequently, the diffusion coefficient can be determined by fitting a linear function to the measured temporal evolution of the variance.

4 Results and discussion

The Gaussian equation (Eq. 4) was used to fit the distribution of the experimental luminescent signal produced by the tagging beam at various instants across a broad pressure range. As an example, Fig. 3 illustrates the evolution over time of the tagged line distribution at a constant pressure of 1 kPa, from the moment of tagging to 500 µs later. The results are normalized by the peak value $S_{\max}(t)$ of the Gaussian distribution. The Gaussian shape flattens over time due to molecular diffusion. To the best of our knowledge, the time range of phosphorescent signal acquisitions presented in this work is the most extensive available in the literature for such a wide range of low pressures.

A regression model was employed to fit the Gaussian equation to the signal distribution, and the quality of the fit was assessed using the coefficient of determination R^2 (Rousson and Goşoniu 2007). The R^2 value can range from 0 to 1, where $R^2 = 1$ indicates a perfect match between experimental data and the fitting function. For Gaussian fitting at each instant and for all pressures investigated, the sample size, $n = 344$, represents the number of pixels along the x-axis direction of the image. In this context, the only independent variable at a given instant is the position x, and the dependent variable is the Gaussian function $f(x, t)$ corresponding to the light intensity profile.

The signal to noise ratio was utilized to estimate the quality of the acquired signal. In this work, the SNR was defined as the ratio between the Gaussian peak $S_{\max}(t)$ and the background emission offset $a_1(t)$ of the image. The overall quality of the experimental data was evaluated based on the R^2 and SNR parameters. Low values of R^2 and SNR indicate that the Gaussian fitting poorly represents the signal distribution, and the intensity of emitted light is too weak to obtain reliable information from the acquired images, respectively.

As an example, Fig. 4 summarizes the temporal evolution of the variance, R^2, and SNR at various instants for four different pressures, ranging from 1 to 8 kPa. It is evident from this figure that both R^2 and SNR decrease over time. Therefore, it was necessary to delimit a time range of confidence in which the acquired dataset's quality could be considered suitable for the entire range of pressures investigated. In the context of extracting the diffusion coefficient from the acetone phosphorescence signal, we have considered that the acquired data remained reliable up to 100 µs after the laser

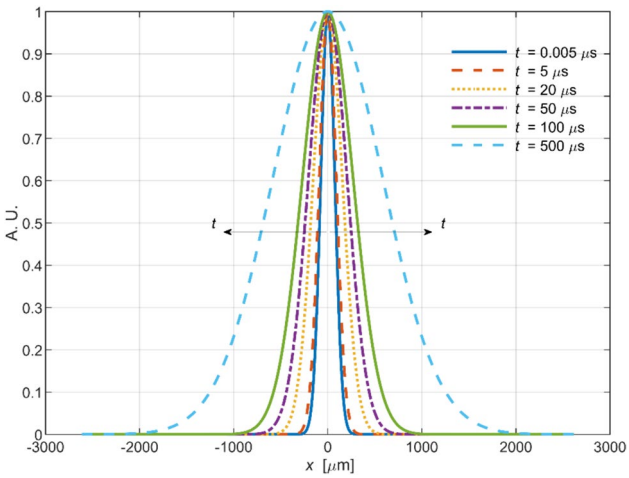

Fig. 3 Gaussian fitting of the temporal evolution of the phosphorescence intensity profile normalized by each Gaussian peak. Experimental data at $p = 1$ kPa

excitation for all experiments, ensuring a minimum SNR of 2.1 and a minimum R^2 of 0.75.

For better analysis, the detail of the variance curves is displayed in Fig. 5, covering a time span up to 300 µs. In accordance with the Einstein-Brownian equation (Eq. 7), at relatively low pressures, the experimental data exhibited a linear evolution of the variance $\sigma_x^2(t)$, from the initial tagging instant up to the designated limit time of 100 µs. However, at higher pressures, a pronounced non-linear behavior of the variance with time was observed immediately after the initial tagging instant (Fig. 5 right column).

The non-linear behavior of the variance with time may be attributed to the occurrence of triplet–triplet annihilation (TTA), which corresponds to non-radiative molecular de-excitation via intermolecular collisions of molecules in the triplet state. The triplet state is a meta-stable energy level reached after excitation, from which a molecule can return to the ground state either by emitting a photon (phosphorescence) or through a non-radiative de-excitation process like TTA. This can be explained by the fact that with increasing pressures at a constant temperature, the gas molecular concentration rises, leading to higher collision frequencies among excited molecules.

The main light-induced reactions of acetone are illustrated in the Jablonski diagram presented in Fig. 6. An acetone molecule (Ac^0) at the ground singlet state S_0 can absorb a photon of high-energy $h\nu$. Subsequently, it transitions to a singlet excited state S_n and promptly relaxes to the first excited state S_1 through internal conversion (IC) and vibrational relaxation (VR):

$$Ac^0 + h\nu \rightarrow Ac^1 \tag{8a}$$

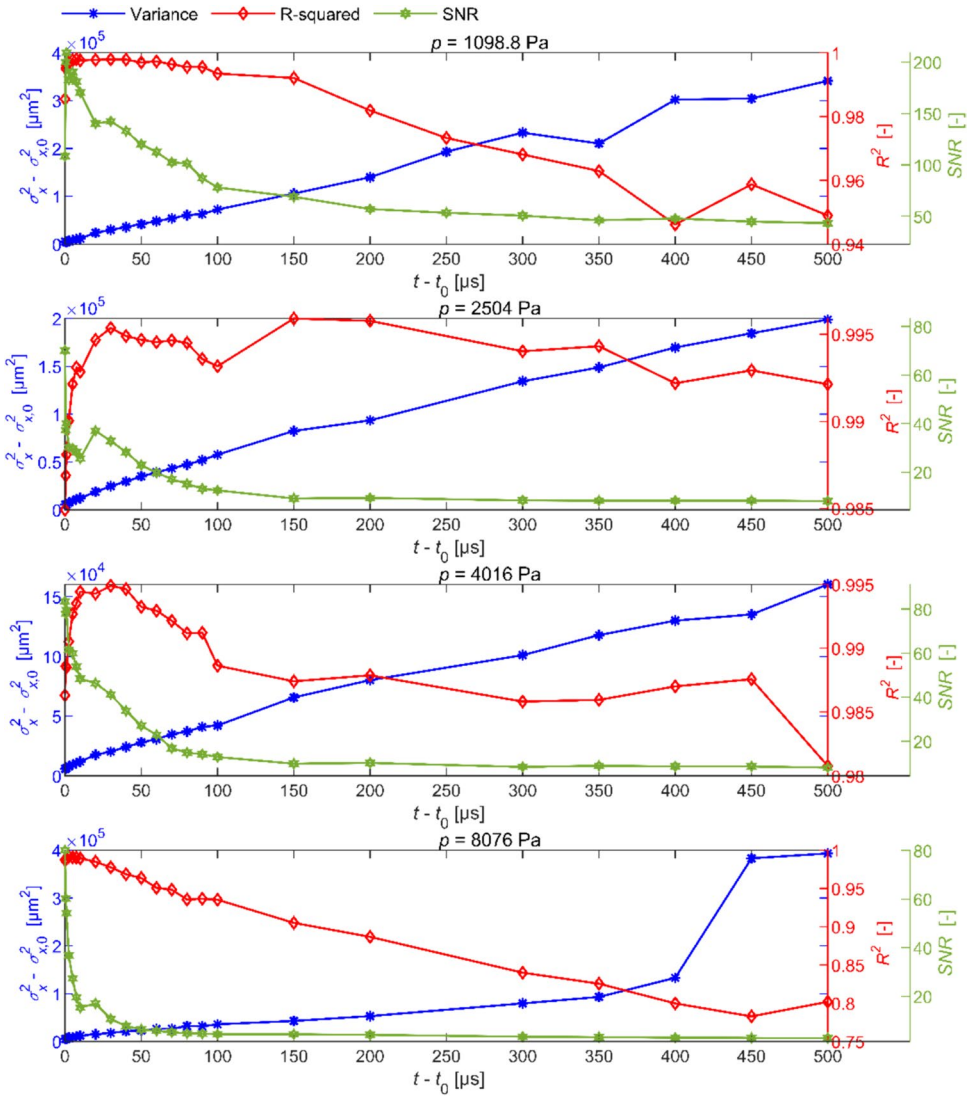

Fig. 4 Temporal evolution of variance (blue lines), R^2 (red lines), and SNR (green lines) at $p = 1$ kPa, 2.5 kPa, 4 kPa and 8 kPa

A first portion of these excited molecules (Ac^1) return to the ground state via non-radiative processes, i.e. without luminescent emission. However, a second portion of Ac^1 return to the ground state via a radiative process, that is by emitting a photon of energy $h\,\nu_f$ in the visible spectrum:

$$Ac^1 \rightarrow Ac^0 + h\,\nu_f \tag{8b}$$

This phenomenon is known as fluorescence. The remaining excited acetone molecules progress to a triplet state T_1 via intersystem crossing, followed by vibrational relaxation:

$$Ac^1 \rightarrow Ac^3 \tag{8c}$$

A fraction of these molecules (Ac^3) in the triplet state return to the ground state by emitting a photon with an energy $h\,\nu_p$:

$$Ac^3 \rightarrow Ac^0 + h\,\nu_p \tag{8d}$$

This process is referred to as phosphorescence.

Another fraction of triplet state molecules can decay to the ground state through non-radiative transitions by IC or VR, or, as previously mentioned, there is the possibility of triplet–triplet annihilation, which occurs when two acetone molecules in the triplet state (Ac^3) interact without releasing any photons:

$$Ac^3 + Ac^3 \rightarrow Ac^0 + Ac^1 \tag{8e}$$

This TTA phenomenon is enhanced by the increase of intermolecular collisions, which is the case here for experiments performed at higher pressures.

To the best of our knowledge, the influence of TTA on the light distribution's evolution over time from an initial Gaussian distribution remains unexplored for acetone. However,

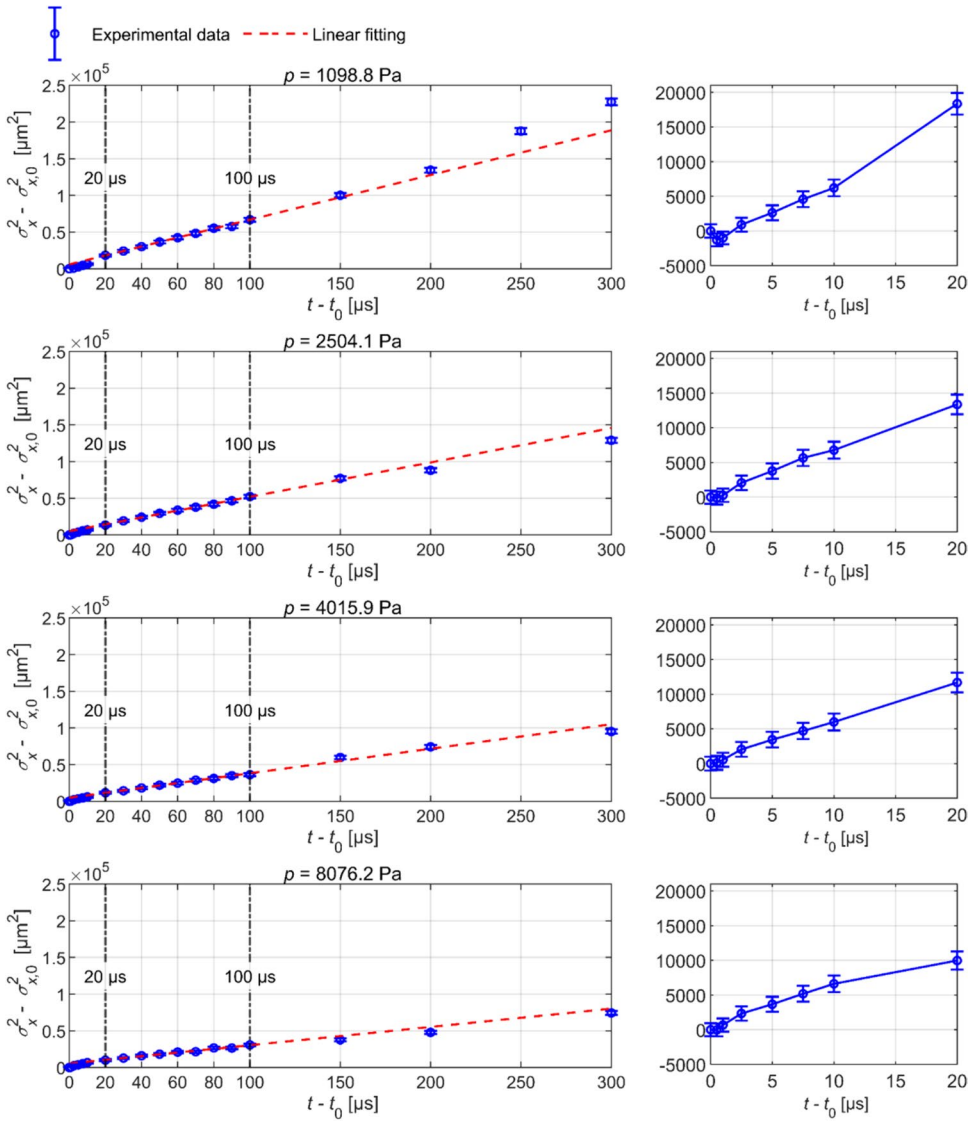

Fig. 5 Temporal evolution of variance (blue circles) and corresponding linear fitting of data between 20 and 100 µs (red dashed line) for different pressures $p = 1$ kPa, 2.5 kPa, 4 kPa and 8 kPa. Left: up to a delay time of 300 µs; Right: zoom on the early delay times up to 20 µs

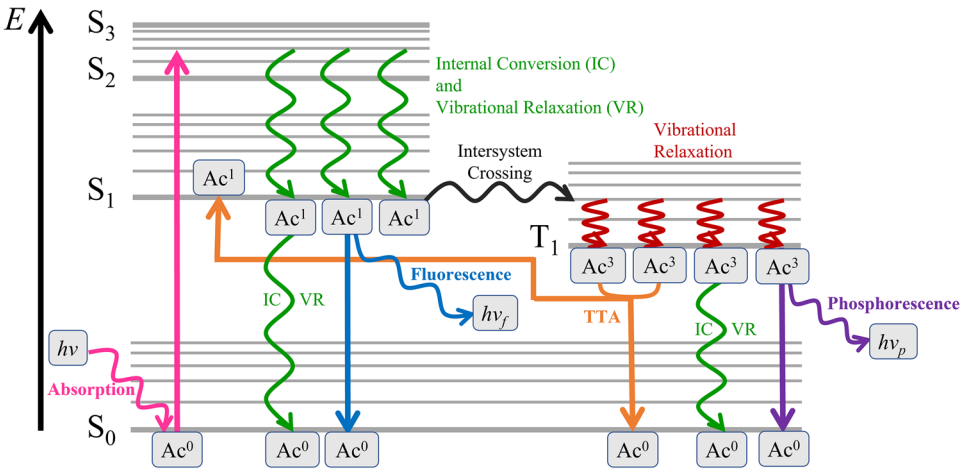

Fig. 6 Jablonski diagram illustrating acetone excitation and deexcitation

some research has been conducted on diacetyl vapor (Bominaar et al. 2008), which can serve as a suitable reference due to its molecular structure similar to that of acetone. In the study conducted by Bominaar et al. (2008), a theoretical model was proposed to predict the light emission distribution following tagging in the case of diacetyl vapor, considering various de-excitation processes, including TTA. The model indicated that TTA affects the Gaussian distribution shape of light emission after laser excitation, resulting in a non-linear variation of the Gaussian variance during the first 50 µs.

Another potential factor to consider is the influence of temperature increase due to molecular absorption by acetone of part of the laser energy. As per Eq. 1, a temperature rise enhances molecular diffusion and consequently accelerates the rate at which the variance increases over time (Bominaar et al. 2008). Our observations align with this prediction, as we noticed a rapid increase in variance immediately after laser excitation. Nonetheless, this effect may only be significant for the first few microseconds post-excitation, given that the temperature rise is limited (Mirzaei et al. 2012) and the excess energy introduced by the laser dissipates rapidly through intermolecular collisions, especially at relatively high pressures.

Our experimental data indicated that the non-linear trend in variance disappeared after a certain time. This was because the diffusion of excited molecules towards the edges of the initial tagged line locally reduced the concentration of triplet molecules, thus weakening the TTA phenomenon. Based on a comprehensive analysis of our dataset and in alignment with the findings of the previous paragraph, it was concluded that the non-linear effects vanished after 20 µs from the laser excitation for the here studied pressure range. This time interval is in agreement with the findings of Mirzaie et al. (2012). Based on these considerations along with those of the previous paragraph, we selected the time range of 20–100 µs following laser excitation as the interval where non-linearity in variance could be considered negligible, and the signal intensity was sufficiently high for the purpose of measuring the signal's variance.

By fitting Eq. 7 to the variance evolution measurements within the 20–100 µs time range (Fig. 5), the self-diffusion coefficient of acetone was extracted across a range of pressures from 0.5 to 10 kPa. This selected time range provided 9 data points for the variance at each pressure, although for the sake of completeness we have included the extended dataset of the measured variance from 5 ns to 300 µs in Fig. 5. The right column of Fig. 5 highlights the non-linear variation in the early delay times, that is in the 0–20 µs time range.

It's worth noting that for delay times greater than 100 µs, the measured variance exhibits larger fluctuations around the linear fitting function. However, within the pre-selected time range of 20–100 µs, the data consistently follow a linear trend.

The uncertainty related to the variance can be deduced from *FWHM* which measurement is obtained via the acquisition of signal in respect to space. The spatial resolution of the measurement depends on the pixel size of the CCD camera, one pixel in this work being 15.2 µm width. In other words, it is possible to define the position x of the signal with an uncertainty $\varepsilon = \pm 7.6\,\mu$m. Since a distance is calculated through the definition of two independent positions, it is possible to define the uncertainty of the beam waist via the propagation of uncertainty principle, as $FWHM = (x_1 - x_2) \pm \sqrt{2}\varepsilon$. By exploiting the relation between *FWHM* and standard deviation (Eq. 7), one can write the same equation as $FWHM = 2\sqrt{2\ln 2}\,\sigma_x \pm \Delta\left(2\sqrt{2\ln 2}\,\sigma_x\right)$ and thus, it is possible to define the uncertainty on the standard deviation as $\Delta\sigma_x = \varepsilon \Big/ \left(2\sqrt{\ln 2}\right)$. From here on the uncertainty on the variance can be written as $\Delta\sigma_x^2(t) = \left|2\,\sigma_x(t)\right|\,\Delta\sigma_x(t)$, while the uncertainty on the variance difference can be computed as $\Delta\left[\sigma_x^2(t) - \sigma_{x,0}^2\right] = \sqrt{\left(\Delta\sigma_x^2(t)\right)^2 + \left(\Delta\sigma_{x,0}^2\right)^2} = 2\Delta\sigma_x\sqrt{\sigma_x^2(t) + \sigma_{x,0}^2}$

The acetone self-diffusion coefficient $D_{2,2}$ was computed based on the slope obtained from a linear fitting of variance against time using the Einstein-Brownian equation (Eq. 7). Thus, the self-diffusion coefficient can be calculated as

$$D_{2,2} = \frac{1}{2}\frac{d\left(\sigma_x^2(t)\right)}{dt} \tag{9}$$

The uncertainties related to this measurement can be estimated from the slope uncertainty estimation. The uncertainty of the slope was determined by calculating an upper and lower border slope as illustrated in Fig. 7. Thus, the uncertainty on the diffusion coefficient was estimated as

$$\Delta D_{2,2} = \frac{D_{2,2\,\max} - D_{2,2\,\min}}{2D_{2,2}} \tag{10}$$

where $D_{2,2\,\max}$ and $D_{2,2\,\min}$ were correlated to the upper and lower border variance to time slopes, respectively.

The experimental results are presented in Fig. 8a and are compared with theoretical predictions obtained from the Chapman-Enskog equation (Eq. 3) using the kinetic diameter values from the literature (Table 1). The data is shown in a logarithmic scale, with dashed lines indicating a $1/p$ dependency of the diffusion coefficient on pressure.

The results indicate that the diffusion coefficients generally decrease with increasing pressure over most of the

pressure range studied. However, the monotonic behavior of $D_{2,2}$ is disrupted at pressures above 6 kPa. For pressure values in the range 1–5 kPa, the measured diffusion coefficients exhibit a linear relationship (in logarithmic scale) with pressure, albeit with a slope that deviates from the Chapman-Enskog theory. Instead of being proportional to p^{-1}, the measured $D_{2,2}$ appears to follow a different power law of pressure, specifically p^a with $-1 < a < 0$.

This unexpected behavior may be attributed to complex intramolecular phenomena occurring following laser excitation, such as TTA, which have not been considered in the diffusion measurements extraction. Nonetheless, the Chapman-Enskog equation was employed to calculate the kinetic diameter d_2 of acetone for each measured diffusion coefficient (Fig. 8b). Since $D_{2,2}$ does not conform to the anticipated trend of $1/p$, d_2 exhibits pressure dependence. However, it is noteworthy that at lower pressures ($p \leq 5$ kPa), the measured d_2 falls within the range of acetone kinetic diameter values reported in the literature. Only at pressures above 6 kPa do the measured $D_{2,2}$ values exceed those calculated using the smallest kinetic diameter available from the literature, i.e. $d = 460$ pm (Fratantonio et al. 2020). The mean value of d_2, obtained from measured kinetic diameters at pressures lower than 6 kPa, is 579 pm, which closely aligns with the predictions of Almy and Anderson (2004), as well as with the average value of all the predictions from the literature, 573 pm. The discrepancies observed in the diffusion coefficients recorded at high pressure may stem from inaccuracies in linear interpolation of the variance time-series. At higher pressures, molecular diffusion is reduced, causing slower variations in the signal profile's variance over time.

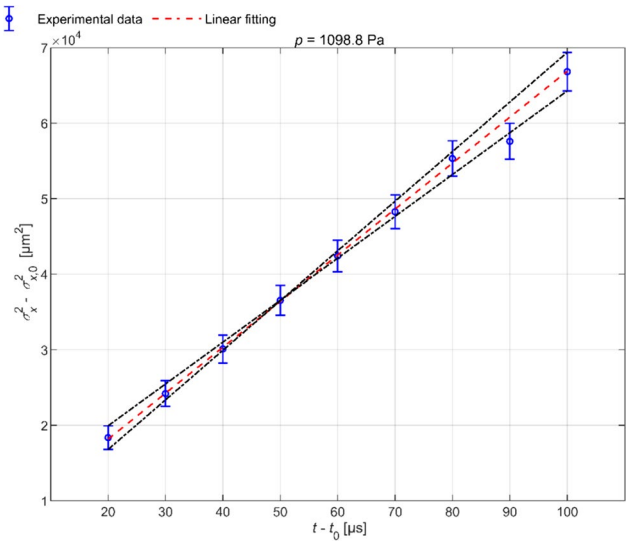

Fig. 7 Illustration of the uncertainty calculation on diffusion by considering the measured slope (red dashed line) and the upper and lower borders (black dotted line) at $p = 1$ kPa

Based on the propagation of uncertainty principle, the relative uncertainty on the kinetic diameter of acetone can be defined as

$$\Delta d_2 = \sqrt{(0.75\ \Delta T)^2 + \left(0.5\ \Delta D_{2,2}\right)^2 + (0.75\ \Delta p)^2} \qquad (11)$$

which depends on the relative uncertainty of the measured diffusion coefficient, temperature, and pressure. The uncertainty on temperature is ±0.5 K at ambient temperature. The uncertainty on pressure is defined as the standard deviation of pressure variation during one image acquisition. The maximum uncertainty value on pressure does not exceed ±1.92 % of the nominal pressure. Thus, as expected, the uncertainty on the kinetic diameter is mainly dominated by the uncertainty on the diffusion coefficient. Table 2 resumes the results obtained in this work, with the respective uncertainty values.

5 Conclusions and perspectives

In this study, we have demonstrated the effectiveness of molecular tagging, an optical technique, for efficiently measuring diffusion coefficients. The data treatment process relies on an uncertainty analysis using R^2 and SNR, leading to the establishment of a rigorous procedure for determining the relevant time range based on theoretical considerations and signal quality. To the best of our knowledge, this research marks the first measurements of self-diffusion coefficients for gaseous acetone using this technique. We explored a pressure range from 500 to 10,000 Pa at room temperature. The obtained diffusion coefficients align well with existing literature data (Si Hadj Mohand et al. 2017; Fratantonio et al. 2020), particularly for pressures below 5 kPa.

However, the measured diffusion coefficients do not conform to the Chapman-Enskog equation, and an alternative power-law relationship between pressure and diffusion coefficient appears to describe the data more accurately. As a result, we observed an unexpected trend in which the kinetic diameter of acetone decreases with increasing pressure, and further investigation will be necessary to confirm or not this observed trend. These findings may help explain the wide range of values registered in the literature over the years. The mean kinetic diameter measured in this work was 579 pm, which closely aligns with the predictions of Almy and Anderson (2004).

At higher pressures ($p > 5$ kPa), our measured values of the diffusion coefficient were higher than those inferred from literature-derived kinetic diameters (Fig. 8a), indicating a kinetic diameter as low as 366 pm (Fig. 8b). In these high-pressure conditions, the triplet–triplet annihilation phenomenon becomes more pronounced. Accurately extracting

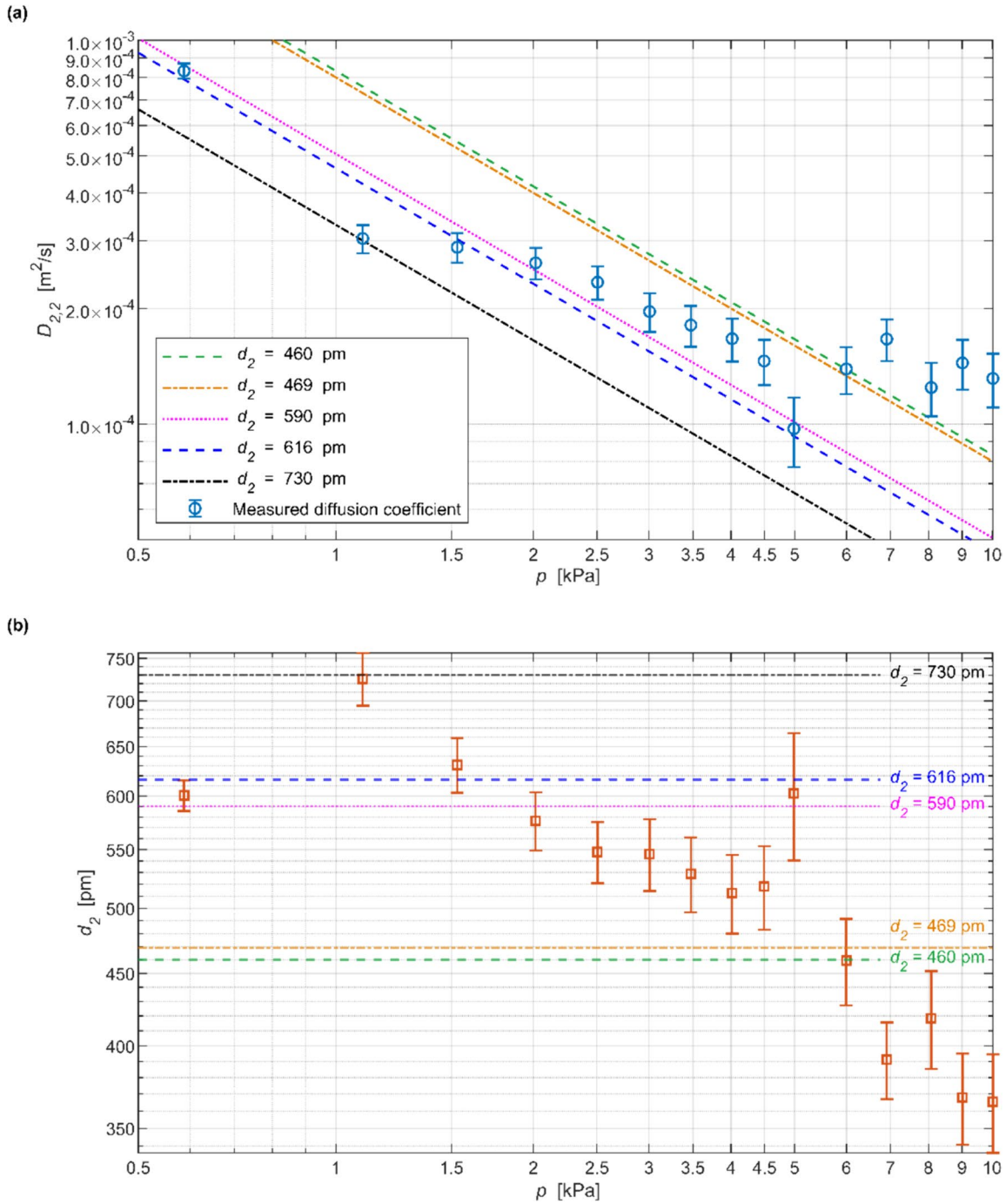

Fig. 8 **a** Measured diffusion coefficient $D_{2,2}$ (blue circles) as a function of pressure compared to theoretical values from the literature (dashed lines) in logarithmic scale; **b** Kinetic diameters d_2 calculated from $D_{2,2}$ by means of the Chapman-Enskog equation (orange squares) as a function of pressure and compared to the values (dashed lines) found in the literature (Table 1) in logarithmic scale

diffusion coefficients from the time evolution of the signal's variance through optical techniques in such conditions may require a more comprehensive model that accounts for key intramolecular processes governing triplet population dynamics. Unfortunately, the Einstein-Brownian formula, even within the time interval where the variance appears to evolve linearly with time, does not capture these complex processes. Further investigation is necessary to determine whether the variation of the kinetic diameter with pressure reflects a genuine physical phenomenon or if it is an error influenced by higher inaccuracies in the data at higher pressures, uncertainties regarding the experimental conditions

Table 2 Measured quantities with corresponding relative uncertainty

$p \pm \Delta p$ [Pa]	$D_{2,2} \pm \Delta D_{2,2}$ [$cm^2\ s^{-1}$]	$d_2 \pm \Delta d_2$ [pm]
587 ± 1.93%	8.32 ± 4.55%	600.5 ± 2.47%
1099 ± 1.33%	3.05 ± 8.46%	725.4 ± 4.28%
1531 ± 0.63%	2.89 ± 8.86%	631.0 ± 4.44%
2016 ± 0.36%	2.63 ± 9.40%	576.4 ± 4.71%
2504 ± 0.41%	2.34 ± 9.92%	548.0 ± 4.97%
3006 ± 0.17%	1.97 ± 11.6%	546.0 ± 5.81%
3475 ± 0.24%	1.81 ± 12.1%	528.9 ± 6.07%
4016 ± 0.05%	1.67 ± 12.7%	512.6 ± 6.37%
4493 ± 0.15%	1.46 ± 13.5%	518.1 ± 6.75%
4988 ± 0.01%	0.97 ± 20.6%	602.4 ± 10.3%
5995 ± 0.04%	1.39 ± 14.0%	459.4 ± 6.99%
6909 ± 0.26%	1.67 ± 12.4%	391.2 ± 6.21%
8076 ± 0.20%	1.25 ± 15.8%	418.4 ± 7.92%
9012 ± 0.18%	1.44 ± 14.8%	368.0 ± 7.39%
10028 ± 0.16%	1.32 ± 15.9%	365.5 ± 7.97%

within the test section, or the need to consider the triplet–triplet annihilation phenomenon for an accurate evaluation of the diffusion coefficient based on the measured variance.

In our future research, we will focus on reducing experimental uncertainties associated with measured diffusion coefficients. This will involve a detailed analysis of the impact of the triplet–triplet annihilation phenomenon and temperature rise in the gas following laser excitation. We plan to investigate these effects numerically. Additionally, we will conduct further studies to directly measure diffusion coefficients within confined spaces, including microchannels, to examine the localized influence of walls on molecular diffusion at the microscale. These measured diffusion coefficient values will then be integrated into the velocity profile reconstruction method, which is essential for the accurate implementation of micro molecular tagging velocimetry.

Acknowledgements We would like to thank Andrea Luccon for his contribution to these results. For the purpose of Open Access, a CC-BY public copyright license has been applied by the authors to the present document and will be applied to all subsequent versions up to the Author Accepted Manuscript arising from this submission.

Author contributions ZZ: investigation, measurement, post-processing and analysis, original draft writing. DF: conceptualization, investigation, validation, formal analysis, review and editing. CBL: supervision, methodology, and resources. MR-C and SC: conceptualization, supervision, methodology, writing, review and editing, and resources.

Funding Open access funding provided by Université Toulouse III - Paul Sabatier.

Data availability Data is provided within the manuscript or supplementary information files.

Declarations

Conflict of interest The authors declare no conflict of interest.

Reference

Almy GM, Anderson S (2004) Lifetime of fluorescence in diacetyl and acetone. J Chem Phys 8:805–814. https://doi.org/10.1063/1.1750584

Arkilic EB, Breuer KS, Schmidt MA (2001) Mass flow and tangential momentum accommodation in silicon micromachined channels. J Fluid Mech 437:29–43. https://doi.org/10.1017/S0022112001004128

Blanc A (1908) Recherches sur les mobilités des ions dans les gaz. J Phys Theor Appl 7:825–839. https://doi.org/10.1051/jphystap:019080070082501

Bominaar J, Pashtrapanska M, Elenbaas T, Dam N, ter Meulen H, van de Water W (2008) Writing in turbulent air. Phys Rev E 77:046312. https://doi.org/10.1103/PhysRevE.77.046312

Bowen TC, Noble RD, Falconer JL (2004) Fundamentals and applications of pervaporation through zeolite membranes. J Membr Sci 245:1–33. https://doi.org/10.1016/j.memsci.2004.06.059

Colin S (2005) Rarefaction and compressibility effects on steady and transient gas flows in microchannels. Microfluid Nanofluid 1:268–279. https://doi.org/10.1007/s10404-004-0002-y

Colin S (2012) Gas microflows in the slip flow regime: a critical review on convective heat transfer. J Heat Trans-T Asme 134:020908. https://doi.org/10.1115/1.4005063

Colin S, Lalonde P, Caen R (2004) Validation of a second-order slip flow model in rectangular microchannels. Heat Transfer Eng 25:23–30. https://doi.org/10.1080/01457630490280047

Colin S, Fernández JM, Barrot C, Baldas L, Bajić S, Rojas-Cárdenas M (1819) Review of optical thermometry techniques for flows at the microscale towards their applicability to gas microflows. Micromachines 2022:13. https://doi.org/10.3390/mi13111819

Einstein A (1956) Investigations on the theory of the Brownian movement. Dover Publications, Mineola

Fratantonio D, Rojas-Cardenas M, Mohand HSH, Barrot C, Baldas L, Colin S (2018) Molecular tagging velocimetry for confined rarefied gas flows: phosphorescence emission measurements at low pressure. Exp Therm Fluid Sci 99:510–524. https://doi.org/10.1016/j.expthermflusci.2018.08.001

Fratantonio D, Rojas-Cárdenas M, Barrot C, Baldas L, Colin S (2020) Velocity measurements in channel gas flows in the slip regime by means of molecular tagging velocimetry. Micromachines 11:374. https://doi.org/10.3390/mi11040374

Frezzotti A, Mohand HSH, Barrot C, Colin S (2015) Role of diffusion on molecular tagging velocimetry technique for rarefied gas flow analysis. Microfluid Nanofluid 19:1335–1348. https://doi.org/10.1007/s10404-015-1649-2

Hu H, Koochesfahani MM (2006) Molecular tagging velocimetry and thermometry and its application to the wake of a heated circular cylinder. Meas Sci Technol 17:1269–1281

Hu H, Zhu J, Yang F, Chen Z, Deng M, Weng L, Ling Y, Zhou Y (2019) A robust etb-type metal–organic framework showing polarity-exclusive adsorption of acetone over methanol for their azeotropic mixture. Chem Commun 55:6495–6498. https://doi.org/10.1039/C9CC02439E

Javed Y, Mansoor M, Shah IA (2019) A review of principles of MEMS pressure sensing with its aerospace applications. Sens Rev 39:652–664. https://doi.org/10.1108/SR-06-2018-0135

Koochesfahani MM, Nocera DG (2007) Molecular tagging velocimetry. In: Tropea C, Yarin AL, Foss JF (eds) Handbook of experimental fluid dynamics. Springer, Berlin, pp 362–382

López Quesada G, Tatsios G, Valougeorgis D, Rojas-Cárdenas M, Baldas L, Barrot C, Colin S (2019) Design guidelines for thermally driven micropumps of different architectures based on target applications via kinetic modeling and simulations. Micromachines 10:249. https://doi.org/10.3390/mi10040249

Maali A, Colin S, Bhushan B (2016) Slip length measurement of gas flow. Nanotechnology 27:374004. https://doi.org/10.1088/0957-4484/27/37/374004

Marrero TR, Mason EA (1972) Gaseous diffusion coefficients. J Phys Chem Ref Data 1:3–118. https://doi.org/10.1063/1.3253094

Mirzaei M, Dam NJ, van de Water W (2012) Molecular tagging velocimetry in turbulence using biacetyl. Phys Rev E 86:046318

Si Hadj Mohand H, Frezzotti A, Brandner JJ, Barrot C, Colin S (2017) Molecular tagging velocimetry by direct phosphorescence in gas microflows: correction of Taylor dispersion. Exp Therm Fluid Sci 83:177–190. https://doi.org/10.1016/j.expthermflusci.2017.01.002

Nadykto AB, Yu F (2003) Uptake of neutral polar vapor molecules by charged clusters/particles: enhancement due to dipole-charge interaction. J Geophys Res Atmospheres. https://doi.org/10.1029/2003JD003664

Otic CJC, Yonemura S (2022) Thermally induced Knudsen forces for contactless manipulation of a micro-object. Micromachines 13:1092

Pitakarnnop J, Varoutis S, Valougeorgis D, Geoffroy S, Baldas L, Colin S (2010) A novel experimental setup for gas microflows. Microfluid Nanofluid 8:57–72. https://doi.org/10.1007/s10404-009-0447-0

Potkay JA (2014) The promise of microfluidic artificial lungs. Lab Chip 14:4122–4138. https://doi.org/10.1039/C4LC00828F

Rehman D, Joseph J, Morini GL, Delanaye M, Brandner J (2020) A hybrid numerical methodology based on CFD and porous medium for thermal performance evaluation of gas to gas micro heat exchanger. Micromachines 11:218

Rojas-Cárdenas M, Graur I, Perrier P, Méolans JG (2015) A new method to measure the thermal slip coefficient. Int J Heat Mass Transf 88:766–774. https://doi.org/10.1016/j.ijheatmasstransfer.2015.05.009

Rousson V, Goşoniu NF (2007) An R-square coefficient based on final prediction error. Stat Methodol 4:331–340. https://doi.org/10.1016/j.stamet.2006.11.004

Samouda F, Colin S, Barrot C, Baldas L, Brandner JJ (2015) Micro molecular tagging velocimetry for analysis of gas flows in mini and micro systems. Microsyst Technol 21:527–537. https://doi.org/10.1007/s00542-013-1971-0

Sharipov F, Seleznev V (1998) Data on internal rarefied gas flows. J Phys Chem Ref Data 27:657–706

Silva E, Rojas-Cardenas M, Deschamps CJ (2016) Experimental analysis of velocity slip at the wall for gas flows of nitrogen, R134a, and R600a through a metallic microtube. Int J Refrig 66:121–132. https://doi.org/10.1016/j.ijrefrig.2016.02.006

Trott WM, Castañeda JN, Torczynski JR, Gallis MA, Rader DJ (2011) An experimental assembly for precise measurement of thermal accommodation coefficients. Rev Sci Instrum 82:035120. https://doi.org/10.1063/1.3571269

Vo DD, Moradi R, Barzegar Gerdroodbary M, Ganji DD (2019) Measurement of low-pressure Knudsen force with deflection approximation for gas detection. Results Phys 13:102257. https://doi.org/10.1016/j.rinp.2019.102257

Zhao L, Wang X, Zhang Z (2023) Numerical investigation into the compression characteristics of a multi-stage Knudsen pump with rectangular channels. Eur Phys J Plus 138:302. https://doi.org/10.1140/epjp/s13360-023-03922-5